Quasi-Deterministic Channel Propagation Model for an Urban Environment at 28 GHz

Neeraj Varshney, Jian Wang, Chiehping Lai, Camillo Gentile, Romain Charbonnier, and Yoann Corre

***Abstract*—We reduced the parameters of the Quasi-Deterministic channel propagation model, recently adopted by the *IEEE 802.11ay* task group for next-generation Wi-Fi at millimeter-wave (mmWave), from measurements collected in an urban environment with our 28 GHz switched-array channel sounder. In the process—as a novel contribution—we extended the clustering of channel rays from the conventional delay and angle domains to the location domain of the receiver, over which the measurements were collected. By comparing channel realizations from the model to realizations from a leading commercial ray-tracer, we demonstrated that the model effects no detriment to accuracy while maintaining the benefit of significantly reduced complexity.**

***Index Terms*—Location clustering, millimeter-wave (mmWave), ray-tracing.**

I. Introduction

Millimeter-wave (mmWave) propagation is characterized by negligible diffraction due to the narrowing of the Fresnel zone [1], [2]. What matters much more at mmWave is diffuse scattering [3], originating from the intricacies of ambient scatterers that appear electrically large at such short wavelengths. In fact, it has been demonstrated that diffuse scattering can account for up to 40% of the total receiver power [3]–[5], yet most mmWave channel propagation models do not model it explicitly but save a few exceptions [3]–[13]. Of particular relevance to this letter is [3] in which *Siradel* [14], in a joint calibration with our team at the National Institute of Standards and Technology, calibrated their *Volcano* 3-D ray-tracing engine against our 28 GHz urban channel measurements.

Although full-scale ray-tracing can deliver a high degree of accuracy, it does not scale to large environments with lots of nodes, for example, for the end-to-end analysis of network throughput and delay. For this reason, the *IEEE 802.11ay* task group [15], developing a new standard for ultrafast (>20 Gb/s) Wi-Fi at mmWave, adopted the Quasi-Deterministic (QD) channel model [11]. In the simplified model, only the line-of-sight (LoS) and specular rays are traced, while the diffuse rays that cluster around the specular rays are generated stochastically. Aside from simplicity, its modular structure has spawned the construction of a library of environments and center frequencies under one framework, each with its own set of model parameters [16], [17].

Manuscript received April 5, 2021; accepted April 14, 2021. Date of publication April 16, 2021; date of current version July 7, 2021. *(Corresponding author: Camillo Gentile.)*

Neeraj Varshney, Jian Wang, Chiehping Lai, and Camillo Gentile are with the National Institute of Standards and Technology, Gaithersburg, MD 20899 USA (e-mail: neeraj.varshney@nist.gov; jian.wang@nist.gov; chiehping.lai@nist.gov; camillo.gentile@nist.gov).

Romain Charbonnier and Yoann Corre are with the Siradel SAS, 35043 Rennes Cedex, France (e-mail: rcharbonnier@siradel.com; ycorre@siradel.com).

Digital Object Identifier 10.1109/LAWP.2021.3073880

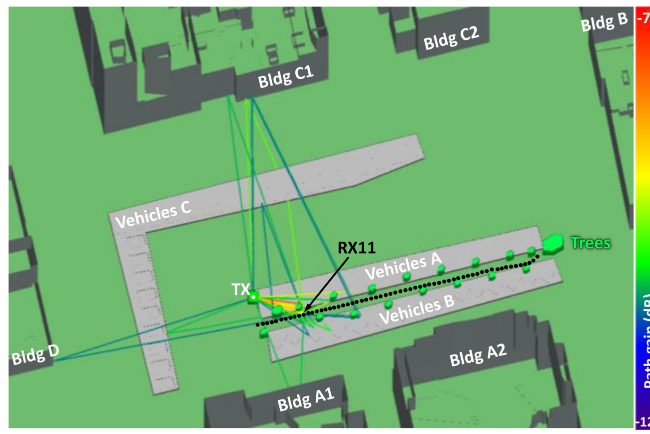

Fig. 1. GIS database of downtown Boulder, Colorado, showing buildings (A1, A2, B, C1, C2, and D), trees, and rows of vehicles (A, B, and C). The 61 RX locations are displayed as black dots and the ray-traced LoS and specular rays between the TX and RX11 are color coded against path gain.

In this letter, we reduce a set of QD model parameters from our 28 GHz urban channel measurements. In Section II, we provide an overview of our channel sounder and the measurement campaign. In Section III, we describe a novel clustering technique—novel in the sense that clustering is extended beyond the conventional delay and angle domains to the location domain of the receiver, over which the measurements were collected—and present the QD model parameters that resulted from the clustering. In Section IV, we validate the QD model demonstrating that, despite its simplicity, its prediction accuracy is comparable to the *Volcano* ray-tracer. Finally, Section V concludes this letter.

II. Measurements

Field measurements were collected with our 28 GHz switched-array channel sounder. The system acquires the complex channel impulse responses (CIRs) between a single dipole transmitter (TX) antenna and 16 horn antennas on a spherical receiver (RX) array. The detail of the system is provided in [3]. The measurement campaign was conducted in downtown Boulder, Colorado, during the month of July. The 3-D geometric information system (GIS) database of the environment is depicted in Fig. 1. The database of the buildings was obtained from OpenStreetMap [18], while the rows of vehicles and trees, represented as simple polygons, were inserted based on pictures/videos captured on site. The stationary TX was mounted

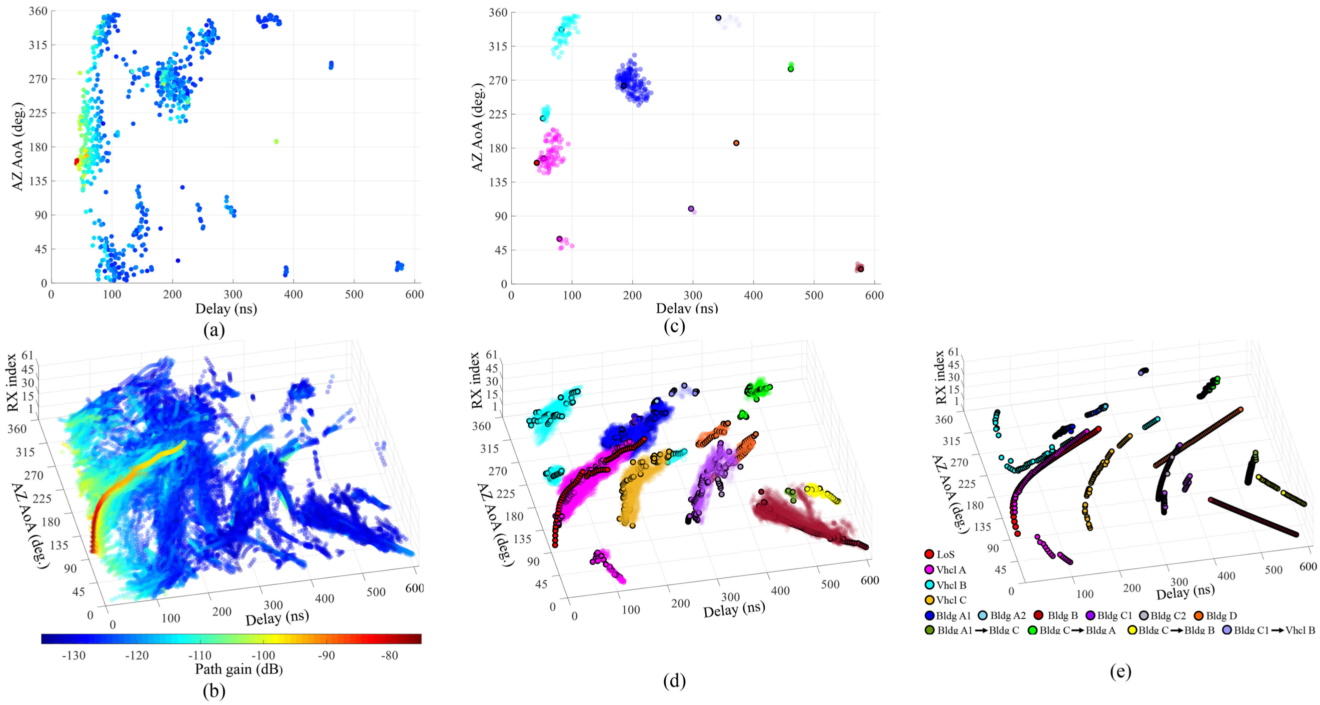

Fig. 2. Channel rays. (a) Measured rays, at illustrative location RX11. (b) Measured rays, across all RXs. (c) Measured rays, at RX11, clustered in different colors, with the LoS and specular rays outlined in black. (d) Measured rays, across all RXs, clustered in different colors, with the LoS and specular rays outlined in black. (e) Predicted LoS and specular rays, across all RXs, classified according to the scatterers that generated the rays (second-order reflections are indicated by arrows).

on a tripod at 2.5 m height; the RX was mounted on the mobile rover at 1.6 m height. The rover enabled the rapid and continuous collection of channel data while recording the location of the RX with centimeter precision. The rover followed a linear trajectory along the sidewalk under a canopy of trees and aligned by vehicles on both sides. The TX–RX distance ranged from 6.1 to 66.1 m, over which 61 *large-scale* channel measurements were collected, shown as black dots, spaced about 1.1 m apart. Each large-scale channel measurement consisted of eight *small-scale* channel acquisitions triggered sequentially, spaced about one wavelength apart (10 mm), producing a rich dataset of 488 total acquisitions.

The 16 CIRs per acquisition were coherently combined through the SAGE super-resolution algorithm [19], [20] to extract a discrete set of measured rays and their properties. The ray properties were extracted in a 4-D domain: path gain, delay, azimuth (AZ) angle-of-arrival (AoA), and elevation (EL) AoA, with average errors of only 1.2 dB, 0.55 ns, 2.70°, and 1.50°, respectively [3]. Any measurement taken with the channel sounder captures not only the channel response but also the response of the sounder itself, i.e., the directional patterns of the antennas and the hardware responses of the TX and RX front ends. Accordingly, SAGE deconvolved the antenna patterns as a part of the algorithm, while the responses of the TX and RX front ends were deconvolved through predistortion filters designed from a back-to-back calibration [21]. Hence, the extracted rays represent the "pristine" response of the channel itself (without the measurement system), thus can be compared directly to ray-tracing predictions. Fig. 2(a) shows the measured rays at an illustrative location RX11, displayed in the delay and AZ AoA domains, and color coded against path gain, and Fig. 2(b) shows the measured rays aggregated across all RXs.

III. QD Model Parameters

The reduction of the QD model parameters from the measured rays is described in this section. First, the rays were clustered jointly in the delay, angle, and—as a novel contribution—location domains. Then, the clusters were classified against the distinct scatterers in the environment that generated them. Finally, the classified clusters were reduced into scatterer-specific model parameters.

A. Location Clustering

Most clustering algorithms are implemented per RX location (e.g., [22]–[25]), hence, in the delay and/or angle domains alone. The drawback is that, as the RX moves, the clusters are subject to the *birth–death* process [26] in which clusters are born (die) when they fall in (out) of the channel sounder's *visibility region*, either due to an occluded scatterer or due to the sounder's limited field-of-view, dynamic range, link budget, etc. Thus, when considering locations singularly, clusters at the edge of the visibility region may appear small and/or weak and get dismissed as noise. Besides the additional domain to better resolve rays, another advantage of clustering in the location domain is spatial consistency, so the output of the algorithm is delay–angle clusters that are already linked across locations. As we shall see later, this is beneficial for cluster classification.

Recently, algorithms that cluster in the location domain have appeared. In [5] and [27], rays are first clustered in delay–angle per location and the resultant cluster heads are, subsequently, tracked over the location. However, because the clustering is still implemented per location in the first step, the birth–death process is not observable. In [28]–[30], the inverse occurs, i.e., rays are first tracked individually in delay–angle over the location and the resultant tracks are, subsequently, clustered based on their similarity. However, the results are simulated based, whereas tracking actual measured rays are highly sensitive to measurement error, diminishing the similarity between the resultant tracks. Moreover, in real measurements, the majority of rays at mmWave are diffuse, which by nature have stochastic delay–angle properties [3]–[5] that effect dissimilarity in their tracks even with no measurement error.

The clustering algorithm we propose considers the delay, angle, and location domains *jointly*, so the birth–death process is observable and can be processed intelligently. Furthermore, the algorithm is applied to real measurements, substantiating its validity. The original version of the proposed algorithm was implemented in the delay–angle only [25]. The proposed algorithm is a direct extension to include location as well, over which the measurements were collected as the RX moved across the 61 locations. The key to the success of the algorithm is the closely and regularly spaced locations (about 1.1 m apart), over which the clusters changed incrementally, i.e., were similar in delay–angle. This enabled the delay–angle clusters to be clustered yet further over the location. Due to space limitations, just an overview of the algorithm is provided in the sequel.

Thanks to negligible diffraction, the mmWave channel is considered sparse and can be represented as the LoS ray, and specular rays surrounded by diffuse rays clustered densely in delay–angle [3]–[5], [11]. Because the number of measured diffuse rays per cluster tended to be low—anywhere between one and eight—the eight small-scale acquisitions per location were aggregated to populate the clusters with more rays for reliable parameter reduction. Exploiting the channel sparsity, the proposed clustering algorithm is based on density filtering through *DBSCAN* [31]. In *DBSCAN*, each measured ray is scanned to determine whether it is surrounded by a least N_m rays within some radius ϵ, using the Euclidean distance in the delay–angle–location domains.[1] If so, the ray is designated as a *core point*. Then, all neighbors (within radius ε) of a core point are designated as *reachable* and kept; otherwise, they are deemed outliers and discarded. The output is clusters of mutually reachable rays. Fig. 2(c) and (d) shows the measured rays clustered in different colors at RX11 and across all RXs, respectively.

B. Cluster Classification

Upon clustering, the (unclustered) LoS ray was identified as the absolute strongest ray per location, the specular rays as the strongest per cluster per location, and the remaining rays as diffuse. The LoS and specular rays identified are outlined in black in Fig. 2(c) and (d). The next step was to classify each cluster against the distinct environment scatterer that generated it. This was accomplished through ray-tracing-assisted predictions at each of the 61 locations in the measurement campaign, exploiting the GIS database in Fig. 1 containing the salient buildings, vehicles, and tree scatterers. Only the LoS and specular rays up to second-order reflections were predicted, as prescribed by the *IEEE 802.11ay* channel model [32], through the method of images [33]. The actual field-of-view of the TX and RX, the dynamic range, and the link budget of the channel sounder were incorporated to obtain predicted rays as comparable as possible to the measured rays. The predicted rays for RX11 are illustrated in Fig. 1, color coded against RX power. These predicted rays are shown across all RXs in Fig. 2(e) and classified in the legend according to their known scatterers. A one-to-one correspondence was found between the predicted (LoS and specular) rays in Fig. 2(e) and the measured (LoS and specular) rays in Fig. 2(d) through visual inspection from which the measured rays were classified according to the scatterers of the corresponding predicted rays.

C. QD Parameter Reduction

From the classified clusters, scatterer-specific QD parameters were reduced. These stochastic parameters describe the strength and shape of the clusters in delay–angle. Specifically, the strength of the cluster's specular ray is gauged through the reflection loss (RL), i.e., its excess loss with respect to free space. The remaining parameters describe the diffuse rays: the *K*-factor (*K*) gauges the relative strength of the cluster's diffuse rays with respect to the specular rays; the AZ and EL root mean square (rms) spreads ($\sigma^{\mathrm{RMS}}_{\mathrm{AZ/EL}}$) describe their shape in the angle domains; and their shape in the delay domain is described by an exponentially decaying envelope (γ) with random fluctuation (σ_S) and by their inter-ray delay (λ). The formal definition of these Rician-distributed parameters is provided in [33], and Table I accordingly compiles the parameter values for the building and vehicle scatterer classes, as identified in Fig. 1. Note that while the trees are depicted in the GIS database, their clusters could not be reliably resolved from the clusters corresponding to buildings A2, B, and C2, and so instead were incorporated as a part of these building scatterer classes. Also, note that buildings C1 and D and vehicle C exhibited diffuse rays too weak to detect and so their clusters were represented by a single specular ray (through the RL parameter alone).

IV. Validation

In this section, we compare the channel realizations of the QD model with channel realizations of the *Volcano* ray-tracer using the measurements as ground truth. The realizations of the QD model were generated by first tracing the LoS ray and specular rays from the scatterer classes in Table I at each of the 61 locations in the measurement campaign, as described in Section III-B. The rays were traced based on the free-space propagation, then the RL from Table I was added to the specular rays. Finally, the diffuse rays were generated per specular ray stochastically from the corresponding parameters in the table according to the algorithm delineated in [33], yielding a set of predicted rays. The algorithm to generate predicted rays from *Volcano* involved distinct diffuse scattering models for building, vehicle, and tree classes, hence is much more elaborate—beyond the scope of this letter—so details are left in [3].

The mean and rms spread of the delay, AZ AoA, and EL AoA, and capacity[2] of the predicted rays from the QD model were computed for each of the 61 locations and subsequently compiled into cumulative distribution functions (CDFs) across all locations. The seven corresponding plots are shown in Fig. 3.

[1]Since the delay, angle, and location domains have different scales and units, they each have to be normalized individually before combining into a composite Euclidean distance. The normalization procedure is described in [5].

[2]Ergodic capacity [35] assuming 0 dBm TX power and omnidirectional RX antenna (to sum over all rays) to compute the RX signal power, and 1 GHz bandwidth to compute the noise power.

TABLE I
QD CHANNEL MODEL PARAMETERS FOR AN URBAN ENVIRONMENT AT 28 GHZ

	Rician parameters	Bldg A1	Bldg A2 (+trees)	Bldg B (+trees)	Bldg C1	Bldg C2 (+trees)	Bldg D	Vhcl A	Vhcl B	Vhcl C
RL (dB)	(v_{RL}, σ_{RL})	(7.04,1.59)	(21.49,1.92)	(12.51,3.60)	(8.35, 1.68)	(18.93,1.90)	(11.87, 2.68)	(21.40,1.93)	(20.05,4.50)	(20.58, 0.93)
K (dB)	($v_{K_{pre}}, \sigma_{K_{pre}}$) ($v_{K_{post}}, \sigma_{K_{post}}$)	(3.23,0.72) (2.43,1.23)	(1.48,3.43) (0.13,1.87)	(1.28,9.21) (1.35,2.11)		(0.18,2.89) (0.13,2.67)		(6.04,1.98) (0.08,1.54)	(0.63,4.79) (0.27,1.81)	
$\sigma_{AZ/EL}^{RMS}$ (deg)	($v_{\sigma_{AZ}^{RMS}}, \sigma_{\sigma_{AZ}^{RMS}}$) ($v_{\sigma_{EL}^{RMS}}, \sigma_{\sigma_{EL}^{RMS}}$)	(7.38,0.91 (2.50,0.82)	(4.61,0.68) (1.89,0.54)	(6.24,2.15) (3.11,1.96)		(6.81,2.12) (2.18,0.57)		(3.16,4.94) (0.38,3.81)	(9.68,2.83) (4.00,1.30)	
γ (ns)	($v_{\gamma_{pre}}, \sigma_{\gamma_{pre}}$) ($v_{\gamma_{post}}, \sigma_{\gamma_{post}}$)	(7.22,2.38) (34.11,7.87)	(0.92,16.35) (1.03,12.84)	(0.37,8.18) (5.62,34.56)		(0.54,13.66) (1.02,22.44)		(14.48,3.31) (1.52,15.53)	(0.62,9.71) (10.56,3.48)	
σ_S (dB)	($v_{\sigma_{S,pre}}, \sigma_{\sigma_{S,pre}}$) $v_{\sigma_{S,post}}, \sigma_{\sigma_{S,post}}$)	(1.45,0.36) (0.84,0.11)	(0.71,0.25) (0.60,0.15)	(0.05,0.58) (0.54,0.10)		(0.73,0.23) (0.61,0.29)		(0.65,0.26) (0.49,0.21)	(0.85,0.24) (0.78,0.22)	
λ (1/ns)	($v_{\lambda_{pre}}, \sigma_{\lambda_{pre}}$) ($v_{\lambda_{post}}, \sigma_{\lambda_{post}}$)	(0.33,0.06) (0.30,0.07)	(0.08,0.04) (0.07,0.08)	(0.00,0.25) (0.12,0.06)		(0.00,0.20) (0.05,0.04)		(0.00,0.14) (0.06,0.04)	(0.10,0.05) (0.16,0.06)	

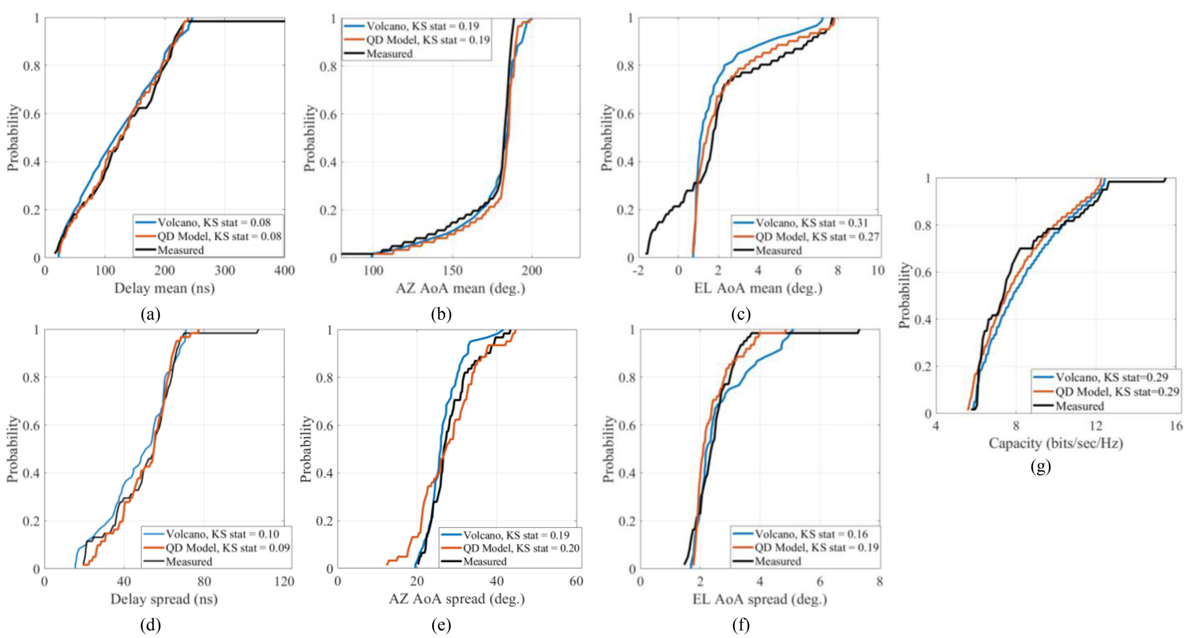

Fig. 3. CDF of the large-scale channel metrics obtained by aggregating measured and predicted rays across all RX locations. (a) Delay mean. (b) AZ AoA mean. (c) EL AoA mean. (d) Delay spread. (e) AZ AoA spread. (f) EL AoA spread. (g) Capacity.

Also shown on the plots are the analogous CDFs for the predicted rays from *Volcano* and for the measured rays. The Kolmogorov–Smirnov (KS) goodness-of-fit test [34] of the QD model CDFs to the ground-truth measured CDFs and of the *Volcano* CDFs to the ground-truth measured CDFs was conducted, yielding the KS statistics displayed in the legends—the value is between 0 and 1 and a lower value indicates a better fit. The KS statistics indicate the fittings are quite comparable; hence, the QD model delivers accuracy comparable to *Volcano*.

The computational complexity of the QD model scales as $O(f^{2r+2})$, where f (=160 in our example) is the number of faces in the GIS database and r (=2) is the highest number of reflections considered. In contrast, the complexity of *Volcano* scales as $O(\Delta\boldsymbol{\theta}^4 \cdot \Delta\boldsymbol{x})$, where $\Delta\boldsymbol{\theta}$ (=6840) is the number of rays launched in the spherical volume of the TX and $\Delta\boldsymbol{x}$ (=17 422) is the number of grid points in the GIS database volume. In short, the QD model is more advantageous when the environment is simplified, i.e., when the number of faces is low.

V. CONCLUSION

Although the accuracy of the QD model was demonstrated as comparable to *Volcano* in the validation conducted, *Volcano* is more elaborate and so more generalizable to environments different than the one measured. For example, the presence of trees is implicit to the scatterer classes in Table I, whereas *Volcano* can deal with trees of any crown shape, height, and leaf density, and placement in the environment since its tree model is so parameterized. Another example is that vehicles in the QD model are treated collectively as a row, whereas Volcano's vehicle model treats each car individually and so is more generalizable to different placements throughout the environment. This generalizability, however, comes at the price of a significant increase in computation and so is stifling when dealing with large complex environments.

REFERENCES

[1] J. Senic, C. Gentile, P. B. Papazian, K. A. Remley, and J.-K. Choi, "Analysis of E-band path loss and propagation mechanisms in the indoor environment," *IEEE Trans. Antennas Propag.*, vol. 65, no. 12, pp. 6562–6573, Dec. 2017.

[2] S. Deng, G. R. MacCartney, and T. S. Rappaport, "Indoor and outdoor 5G diffraction measurements and models at 10, 20, and 26 GHz," in *Proc. IEEE Global Commun. Conf.*, 2016, pp. 1–7.

[3] R. Charbonnier *et al.*, "Calibration of ray-tracing with diffuse scattering against 28-GHz directional urban channel measurements," *IEEE Trans. Veh. Technol.*, vol. 69, no. 12, pp. 14264–14276, Dec. 2020.

[4] C. Gentile, P. B. Papazian, R. Sun, J. Senic, and J. Wang, "Quasi-deterministic channel model parameters for a data center at 60 GHz," *IEEE Antennas Wireless Propag. Lett.*, vol. 17, no. 5, pp. 808–812, May 2018.

[5] C. Lai, R. Sun, C. Gentile, P. B. Papazian, J. Wang, and J. Senic, "Methodology for multipath-component tracking in millimeter-wave channel modeling," *IEEE Trans. Antennas Propag.*, vol. 67, no. 3, pp. 1826–1836, Mar. 2019.

[6] X. Lin, B. Ai, D. He, K. Guan, C. Zhao, and Z. Zhong, "Angular spread characteristics in high-speed railway scenarios in millimeter-wave band," in *Proc. 12th Eur. Conf. Antennas Propag.*, 2018, pp. 1–5.

[7] C. Zheng, Z. Xu, D. He, K. Guan, B. Ai, and J. M. García-Loygorri, "Millimeter-wave channel measurement based ray-tracing calibration and analysis in metro," in *Proc. IEEE Int. Symp. Antennas Propag. USNC-URSI Radio Sci. Meeting*, Jul. 2019, pp. 1–2.

[8] D. He *et al.*, "Channel measurement, simulation, and analysis for high-speed railway communications in 5G millimeter-wave band," *IEEE Trans. Intell. Transp. Syst.*, vol. 19, no. 10, pp. 3144–3158, Oct. 2018.

[9] D. He *et al.*, "Influence analysis of typical objects in rural railway environments at 28 GHz," *IEEE Trans. Veh. Technol.*, vol. 68, no. 3, pp. 2066–2076, Mar. 2019.

[10] L. Wang *et al.*, "Vehicle-to-infrastructure channel characterization in urban environment at 28 GHz," *China Commun.*, vol. 16, no. 2, pp. 36–48, Feb. 2019.

[11] A. Maltsev *et al.*, "Quasi-deterministic approach to mmwave channel modeling in a non-stationary environment," in *Proc. IEEE Globecom Workshops*, Dec. 2014, pp. 966–971.

[12] B. Ai *et al.*, "On indoor millimeter wave massive MIMO channels: Measurement and simulation," *IEEE J. Sel. Areas Commun.*, vol. 35, no. 7, pp. 1678–1690, Jul. 2017.

[13] K. Guan *et al.*, "Towards realistic high-speed train channels at 5G millimeter-wave band—Part I: Paradigm, significance analysis, and scenario reconstruction," *IEEE Trans. Veh. Technol.*, vol. 67, no. 10, pp. 9112–9128, Oct. 2018.

[14] Siradel. [Online]. Available: https://www.siradel.com/

[15] IEEE P802.11 - Task Group ay. [Online]. Available: https://www.ieee802.org/11/Reports/tgay_update.htm

[16] Mathworks. [Online]. Available: https://www.mathworks.com/help/wlan/ref/wlantgaychannel-system-object.html

[17] A. Bodi *et al.*, "NIST quasi-deterministic (Q-D) channel realization software," 2020. [Online]. Available: https://github.com/wigig-tools/qd-realization

[18] OpenStreetMap Project, 2020. [Online]. Available: www.openstreetmap.org

[19] K. Hausmair, K. Witrisal, P. Meissner, C. Steiner, and G. Kail, "SAGE algorithm for UWB channel parameter estimation," in *Proc. COST 2100 Manage. Committee Meeting*, 2010, pp. 1–7.

[20] P. B. Papazian *et al.*, "Calibration of millimeter-wave channel sounders for super-resolution multipath component extraction," in *Proc. 10th Eur. Conf. Antennas Propag.*, 2016, pp. 1–5.

[21] R. Sun *et al.*, "Design and calibration of a double-directional 60 GHz channel sounder for multipath component tracking," in *Proc. 11th Eur. Conf. Antennas Propag.*, 2017, pp. 3336–3340.

[22] C.-C. Chong, C.-M. Tan, D. L. Laurenson, S. McLaughlin, M. A. Beach, and A. R. Nix, "A new statistical wideband spatio-temporal channel model for 5-GHz band WLAN systems," *IEEE J. Sel. Areas Commun.*, vol. 21, no. 2, pp. 139–150, Feb. 2003.

[23] C. Gentile, S. M. Lopez, and A. Kik, "A comprehensive spatial-temporal channel propagation model for the ultrawideband spectrum 2–8 GHz," *IEEE Trans. Antennas Propag.*, vol. 58, no. 6, pp. 2069–2077, Jun. 2010.

[24] R. He *et al.*, "On the clustering of radio channel impulse responses using sparsity-based methods," *IEEE Trans. Antennas Propag.*, vol. 64, no. 6, pp. 2465–2474, Jun. 2016.

[25] J. Wang, C. Gentile, J. Senic, R. Sun, P. B. Papazian, and C. Lai, "Unsupervised clustering for millimeter-wave channel propagation modeling," in *Proc. IEEE 86th Veh. Technol. Conf.*, 2017, pp. 1–4.

[26] A. F. Molisch, H. Asplund, R. Heddergott, M. Steinbauer, and T. Zwick, "The COST259 directional channel model—Part I: Overview and methodology," *IEEE Trans. Wireless Commun.*, vol. 5, no. 12, pp. 3421–3433, Dec. 2006.

[27] J. Salo, J. Salmi, and P. Vainikainen, "Automatic clustering of nonstationary MIMO channel parameter estimates," in *Proc. Int. Conf. Telecommun.*, 2005, pp. 1–5.

[28] C. Huang, R. He, Z. Zhong, Y.-A. Geng, Q. Li, and Z. Zhong, "A novel tracking-based multipath component clustering algorithm," *IEEE Antennas Wireless Propag. Lett.*, vol. 16, pp. 2679–2683, 2017.

[29] Q. Zheng, R. He, and C. Huang, "A tracking-based multipath components clustering algorithm," in *Proc. 2nd URSI Atlantic Radio Sci. Meeting*, 2018, pp. 1–4.

[30] C. Huang, A. F. Molisch, Y.-A. Geng, R. He, B. Ai, and Z. Zhong, "Trajectory-joint clustering algorithm for time-varying channel modeling," *IEEE Trans. Veh. Technol.*, vol. 69, no. 1, pp. 1041–1045, Jan. 2020.

[31] M. Ester, H.-P. Kriegel, J. Sander, and X. Xu, "A density-based algorithm for discovering clusters in large spatial databases with noise," in *Proc. 2nd Int. Conf. Knowl. Discovery Data Mining*, 1996, vol. 96, no. 34, pp. 226–231.

[32] Mentor.ieee.org. "IEEE P802.11 Wireless LANs: Channel Models for IEEE 802.11ay," [Online]. Available: https://mentor.ieee.org/802.11/dcn/15/11-15-1150-09-00ay-channel-models-for-ieee-802-11ay.docx

[33] M. Lecci *et al.*, "Quasi-deterministic channel model for mmWaves: Mathematical formalization and validation," in *Proc. IEEE Globecom*, Dec. 2020, pp. 1–6.

[34] F. J. Massey, "The Kolmogorov-Smirnov test for goodness of fit," *J. Amer. Statist. Assoc.*, vol. 46, no. 253, pp. 68–78, 1951.

[35] A. Goldsmith, *Wireless Communications*. Cambridge, U.K.: Cambridge Univ. Press, 2005.